Int J Adv Manuf Technol (2013) 65:81–95
DOI 10.1007/s00170-012-4152-x

ORIGINAL ARTICLE

Cutting torque and tangential cutting force coefficient identification from spindle motor current

Saurabh Aggarwal · Nenad Nešić · Paul Xirouchakis

Received: 13 December 2011 / Accepted: 9 April 2012 / Published online: 11 May 2012

Abstract This article presents an enhanced methodology for cutting torque prediction from the spindle motor current, readily available in modern machine tool controllers. This methodology includes the development of the spindle power model which takes into account all mechanical and electrical power losses in a spindle motor for high-speed milling. The predicted cutting torque is further used to identify tangential cutting force coefficients in order to predict accurately the cutting forces and chatter-free regions for milling process planning purposes. The developed model is compared with other studies available in the literature, and it demonstrates significant improvements in terms of the completeness and accuracy achieved. The developed model is also validated experimentally, and the obtained results show good compliance between the predicted and the measured cutting torque. The developed enhanced procedure is very appealing for industrial implementation for cutting torque/force monitoring and tangential cutting force coefficient identification.

Keywords Cutting torque · Spindle power modeling · Spindle motor current · Cutting force coefficients · High-speed milling

S. Aggarwal (✉) · N. Nešić · P. Xirouchakis
Laboratory of Computed Aided Design and Production (LICP),
Swiss Federal Institute of Technology, Lausanne (EPFL),
STI-IGM-LICP, ME B1 344, Station 9,
1015 Lausanne, Switzerland
e-mail: saurabh.aggarwal@epfl.ch

N. Nešić
e-mail: nenad.nesic@epfl.ch

P. Xirouchakis
e-mail: paul.xirouchakis@epfl.ch

1 Introduction

In the highly competitive economic environment, modern manufacturing industries face many challenges in order to achieve high productivity. To meet these challenges, many studies are conducted to predict the cutting forces and chatter-free regions during the milling process by mathematical modeling [1, 2]. High cutting forces and unstable milling lead to high vibration, poor surface quality, and reduction in spindle and cutting tool life, thus affecting the overall productivity.

Cutting force coefficients are needed for accurate prediction of the cutting forces and chatter-free regions during the milling process [3]. They must be experimentally determined from cutting force measurements for a given combination of cutting tool geometry and workpiece material [4].

In the standard procedure, the cutting force coefficients are identified from average values of the cutting force components measured by a cutting force dynamometer in slot cutting experiments at different feed rates [5, 6]. This experimental setup is impractical in modern shop floors due to its high cost and hardware setup complexity. Therefore, there is a constant need in industry for simple and efficient procedures for cutting force coefficient identification.

Tangential cutting force coefficients, which are the most significant for cutting force and chatter-free region prediction, can be obtained from the cutting torque measured directly on a spindle by using piezoelectric torque dynamometers or capacitance spindle displacement sensors [7]. However, these approaches are also plagued with practical problems, such as heat generated by the spindle motor (in the case of the built-in torque sensor), variable sensitivity throughout the machine tool power range, complicated assembly and, again, high costs.

To overcome these problems in cutting force/torque determination, a simple and cost-effective solution is found in using built-in current sensors for motion control in servo

motors. When a change of the mechanical load on the motor occurs, the motor current is modified by the servo controller to overcome it. In modern CNC machine tools, the motor current can be digitally output to external signal acquisition systems.

Current sensors of feed-axis servo motors can be used for the calculation of force components normal to the machined surface [8]. However, due to the high influence of friction forces in feed-axis servo drives, the application of this method for cutting force component determination is limited to discrete monitoring in specific locations where friction influence can be predicted sufficiently accurately.

On the other hand, cutting torque can be calculated relatively easily from the spindle current due to the smaller magnitude of friction forces and constant operational speed [7]. Dunwoody [9] has proposed a procedure for the indirect identification of tangential cutting force coefficients (K_{tc} and K_{te}) from the cutting torque. Instead of being measured directly, the cutting torque is obtained from a difference in spindle power consumption in material cutting and air cutting. The spindle motor current, measured by a built-in load meter, is proportional to the total power spent by the spindle, which is expressed as:

$$I = K_{lm} P_{ACeff} \tag{1.1}$$

where I is the spindle current proportional to the total spindle power (useful power, spent on cutting plus losses measured by a built-in load meter and obtained from the controller), K_{lm} is the load meter constant, and P_{Aceff} is the effective power from the electrical network.

In Dunwoody's model, the total power spent by the spindle is calculated as the product of the spindle angular speed (ω_M) and the sum of torques that the spindle has to overcome as

$$I = K_{lm} \omega_M (T_{cut} + b\omega_M + T_{cf}) \tag{1.2}$$

where T_{cut} is the cutting torque, $b\omega_M$ is the torque needed to overcome viscous friction, and T_{cf} is the torque needed to overcome Coulomb friction.

For air cutting (T_{cut}=0), the measured spindle motor current accounts only for power losses. It is derived from Eq. 1.2

$$I_f = K_{lm} b \omega_M^2 + K_{lm} T_{cf} \omega_M \tag{1.3}$$

where I_f is the spindle current proportional to the power loss. This model is simple and efficient, but does not take into account the dependency of Coulomb friction losses on spindle speed, which is especially important in the case of high-speed machining [10]. Furthermore, this model does not include, at least explicitly, the electric losses in the spindle motor.

In the present work, the model for total spindle power estimation is improved in terms of including all mechanical and electrical sources of power loss in the spindle drive.

Figure 1 illustrates a typical modern motorized spindle with a simplified presentation of all mechanical torques that it has to overcome while rotating: friction in bearings, T_{fBi} (i=1, 2…); cutting torque, T_{cut}; and windage friction torque, T_{vw}.

The Coulomb friction is generally dependent on material characteristics and normal forces in the friction contact, while the viscous friction is dependent on the speed of relative motion of bodies in contact and the properties of the fluid film that separates them. In order to sustain the combined radial and axial load, the bearings in motorized spindles are typically featured as pairs of angular contact ball bearings. The first general load deflection analysis of angular contact bearings, including the influence of centrifugal forces on balls and gyroscopic effects, was developed by Jones [11]. Palmgren [12] has provided empirical expressions for viscous friction torque in the bearings. The study performed by Houpert [13] included elements of Hertzian theory to determine the geometrical properties of the contact zone and pressure distribution in the fluid, but did not take into account the centrifugal and gyroscopic effects on rolling elements. The most comprehensive analytical study of Coulomb and viscous friction in bearings is given by Harris [14].

The low-friction properties of angular contact bearings are of special importance in high-speed machining. The value of contact angles between the balls and the rings in such a design is a function of dynamic variables in operational conditions. Antoine et al. [15] have developed a procedure for the explicit angle calculation in angular contact ball bearings.

The windage friction torque originates in the air gap between the rotor and stator due to the dynamic viscosity of the air. This problem has been analyzed by Bossmanns and Tu [16]. Besides the mechanical losses, the power flow in motorized spindles also includes different types of losses due to electrical phenomena in the spindle motor. This power flow is illustrated in Fig. 2.

Although extensive research has been conducted in the last three decades, the electrical power losses are still not completely explained by theoretical models in a comprehensive manner. Jordan [17] and Hughes [18], among others, explain the phenomena that cause different types of electrical losses. Bossmans [19] provides some semi-empirical expressions to calculate motor core and copper losses, while Köfler [20] and Agamloh [21] report some experimental and empirical results of stray loss estimation.

In this paper, a holistic model for total spindle power calculation is presented. This model is inspired by the aforementioned research results and features some enhancements in terms of the generality and derivation of all geometric, kinematic, and dynamic variables that appear in the developed model. Furthermore, it expresses all sources of power loss as a function of spindle angular speed and mechanical

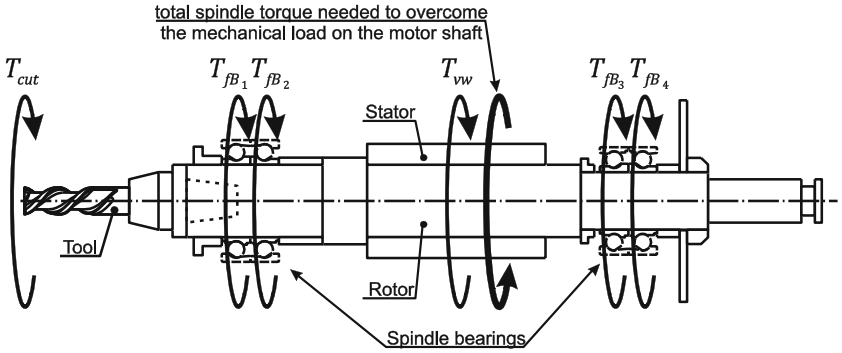

Fig. 1 Free body diagram of a motorized spindle

load on the spindle shaft, which allows for easy experimental validation and practical implementation.

The enhanced procedure for cutting torque and tangential cutting force coefficients identification from spindle motor current consists of four steps:

1. Development of a holistic theoretical model for total spindle power calculation that includes the power loss due to the spin-related friction torque in the spindle bearings, the power loss due to the windage friction torque, and electrical losses in the spindle motor
2. Air cutting tests at different spindle speeds (spindle motor current measurement) and slot cutting tests at different spindle speeds (spindle motor current and cutting torque measurement)
3. Development of an empirical model for cutting torque prediction as a function of the spindle rotational speed and spindle current
4. Slot cutting tests at different feed rates for validation of the cutting torque prediction model and the identification of tangential cutting torque coefficients:
   (a) Spindle current measurement (for cutting torque prediction),
   (b) Direct cutting torque measurement with a torque dynamometer (for comparison and validation of the procedure)

The content of the article is organized as follows. In Section 2, the detailed model of the total power spent by the spindle motor is presented. The mathematical expressions for all modeled mechanical and electrical losses are presented in this section, while some more detailed derivations are provided in the Appendix. The experiments performed to identify the parameters in the empirical model are demonstrated in Section 3, along with the results and accuracy obtained. An industrial implementation of the model, for tangential cutting force coefficient identification, is presented in Section 4. This section is followed by conclusions on the important contributions of the presented research work.

2 Theoretical model for the total spindle power calculation

Motorized spindles of modern machine tools typically use alternate current (AC) induction motors. Therefore, the expressions for mechanical and electrical losses estimation presented in the further text will correspond only to AC induction motors.

The total power, P_{AC} (in watts), drawn by a symmetrical three-phase induction motor from the electrical network is calculated by the following expression:

$$P_{\mathrm{AC}} = \sqrt{3}UI \tag{2.1}$$

where U is the voltage and I is the current. Only a portion of the total power, termed as effective electric input power, P_{ACeff} (in watts), is actually used for overcoming mechanical losses or dissipated as heat. It is expressed as:

$$P_{ACeff} = \sqrt{3}UI|\cos\varphi| \tag{2.2}$$

In Eq. 2.2, $\cos\varphi$ represents the power factor (φ is the phase angle between the vectors of voltage and the current). In modern electric motor designs, automatic power factor correction units are implemented to achieve $|\cos\varphi| = 1$, thus reducing transmission losses and improving voltage regulation.

The total power (in watts) used by a motorized spindle to overcome the mechanical load and compensate for

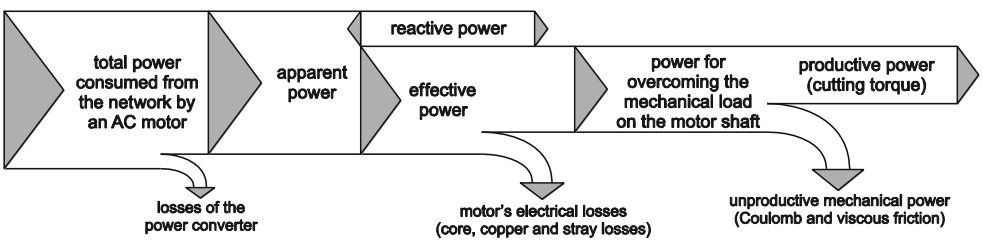

Fig. 2 Power flow in a motorized spindle

mechanical and electrical losses in the system is expressed by summing up the following components:

$$P_{ACeff} = P_{\text{cut}} + P_{\text{ml}} + P_{\text{el}} \tag{2.3}$$

where

- $P_{\text{cut}} = T_{cut}\omega_M$ is the power providing the cutting torque, T_{cut}, needed to overcome tangential cutting force in the tool/part contact at a spindle rotational speed, ω_{M} (per second)
- P_{m1} and P_{e1} represent the total mechanical and electrical power losses, respectively, in the spindle drive system.

2.1 Mechanical losses in a motorized spindle

Total mechanical losses in the motorized spindle are the consequence of the Coulomb and viscous friction phenomena in contact areas due to the relative motions of the members of kinematic pairs. The total torque required to overcome all sources of mechanical power loss in a motorized spindle is expressed as

$$T_{ml} = \frac{P_{ml}}{\omega_M} = T_\mu + T_v \tag{2.4}$$

where T_μ is the torque to overcome the Coulomb friction forces and T_v is the torque to overcome the viscous friction forces. This equation is further decomposed according to the physical sources of friction loss into

$$T_{ml} = T_{\text{B}\mu\text{l}} + T_{\text{B}\mu\text{s}} + T_{\text{B}v} + T_{v\text{w}} \tag{2.5}$$

where $T_{\mu\text{l}}$ is the load-related friction torque in spindle bearings, $T_{\mu\text{s}}$ is the spin-related friction torque in spindle bearings, $T_{\text{B}v}$ is the viscous friction torque in spindle bearings, and $T_{v\text{w}}$ is the windage friction torque in the air gap between the stator and the rotor.

2.1.1 Load-related friction torque in spindle bearings, $T_{B\mu l}$

The dependency of friction losses in bearings on both load and velocity is of great importance in high-speed machining analyses. Angular contact ball bearings are commonly used in motorized spindles. The most comprehensive theoretical bearing friction model is given by Harris [14].

Bearing friction torque due to the applied load is calculated as

$$T_{\text{B}\mu\text{l}} = f_{\text{l}} F_\alpha d_{Bb} \tag{2.6}$$

where f_{l} is a unitless factor depending upon the bearing design and relative bearing load, F_α is contact angle-related load (newton), and d_{Bb} is the diameter of a bearing that corresponds to the centers of the balls (in millimeters).

Bearing friction torque due to the applied load can be calculated analytically/numerically. It does not depend on spindle speed, but it is strongly dependent on the bearing geometry and type. The power needed to overcome the bearing friction torque due to the applied load is expressed as

$$P_{\text{B}\mu\text{l}} = T_{\text{B}\mu\text{l}}\omega_M = f_{\text{l}} F_\alpha d_{Bb}\omega_M \tag{2.7}$$

Equation 2.7 is simplified to describe the power needed to overcome the bearing friction torque due to the applied load.

$$P_{\text{B}\mu\text{l}} = K_{\text{B}\mu\text{l}}\omega_M \tag{2.8}$$

where $K_{\text{B}\mu\text{l}}$ is an applied load constant.

For ball bearings, the factor f_{l} can be calculated by using the following expression [14]:

$$f_{\text{l}} = z\left(\frac{F_s}{C_s}\right)^y \tag{2.9}$$

where z and y are constants depending on the ball bearing contact angles. For nominal contact angles between 30° and 40° in angular contact ball bearings, the values of these coefficients are z=0.001 and y=0.33 [14]. F_s and C_s are the static equivalent load and the basic static load (both in newton), respectively.

The basic static load, C_{s}, is approximated by using

$$C_s = \phi_s i Z d_{\text{b}}^2 \cos\alpha \tag{2.10}$$

where

- φ_{s} is a unitless parameter depending on the following ratio, γ_{b}:

$$\gamma_b = \frac{d_b \cos\alpha}{d_{Bb}} \tag{2.11}$$

- i is the number of rows of rolling elements,
- Z is the number of balls per bearing,
- d_{b} is the ball diameter (in millimeters),
- α is the ball bearing contact angle (radian)

Static equivalent load is equal to the radial load at radial bearings and to the axial load at thrust bearings. For angular contact ball bearings, it is calculated by using

$$F_s = \max(X_{\text{s}}F_r + Y_s F_a, F_r) \tag{2.12}$$

where X_{s} and Y_{s} are constants depending on the ball bearing contact angle, F_{r} is the radial load (in newton), and F_{a} the is axial load (in newton).

Values of C_{s} are generally given in manufacturers' catalogues along with the data to enable the calculation of F_{s} [14]. Contact angle-related load can be calculated by using the following expression:

$$F_\alpha = \max(0.9F_a\cot\alpha - 0.1F_r, F_r) \tag{2.13}$$

The notion of the *bearing contact angle* needs to be explained in detail because its value depends on the work conditions of the bearing. The derivations of expressions for the calculation of the dynamic values of the bearing contact angle are given in the Appendix.

2.1.2 The spin-related friction torque, $T_{B\mu s}$

When a rolling element rotates relative to a deformed surface in the contact areas with raceways, instead of a simple rolling motion, a combination of rolling and sliding motions of the rolling element is generated. Additionally, in the case of angular contact ball bearings, due to the gyroscopic effect, the rolling motion does not occur exactly on a line parallel to the raceway. As a consequence, an additional motion occurs: the "spinning" rotation of the ball. It represents the pure sliding in the contact area, thus contributing significantly to the overall bearing friction power loss.

Detailed analysis of this problem is given by Harris [14]; here, the main conclusions from [14] are applied to the case of spindle bearings. Two variables, the angular speed of ball spinning and the corresponding friction torque, are determined in order to calculate the power loss due to the ball spinning phenomenon.

Figure 3 illustrates the speed vector for a single ball in a bearing. The pitch angle β is a consequence of the angular contact bearing design, whereas the yaw angle β' is a consequence of the existence of the gyroscopic motion. The other variables are represented in Fig. 3:

- ω_b is the vector of the resultant angular velocity of the ball (composed of the rolling, sliding, and spinning motion components)
- x is the axis of the bearing rotation
- ψ is the current angular position of the ball in the bearing

The angular speed of spinning for a ball in the bearing ω_{spin} can be calculated using the following expression [14]:

$$\omega_{spin} = \omega_M \left(\frac{1 - \gamma_b' \cos\alpha_i}{\gamma_b'} \tan(\alpha_i - \beta) + \sin\alpha_i \right) \tag{2.14}$$

where

- ω_M is the angular speed of the motor (spindle) shaft
- α_i and α_o are the dynamic values of the bearing contact angle corresponding to the inner and outer raceways, respectively (see Fig. 11b)
- γ_b' is a geometric parameter that defines the ratio between the ball diameter, d_b, and the bearing diameter corresponding to ball centers, d_{Bb},

$$\gamma_b' = \frac{d_b}{d_{Bb}} \tag{2.15}$$

- β is the pitch angle (see Fig. 3) defined as

$$\beta = \arctan\left(\frac{\sin\alpha_o}{\cos\alpha_o + \gamma_b'} \right) \tag{2.16}$$

Assuming that the gyroscopic motion can be neglected and that the spinning occurs in the center of the contact surface between the ball and the inner raceway, Harris [14] derives the following expression for the spinning torque on the inner/outer (i/o) raceway:

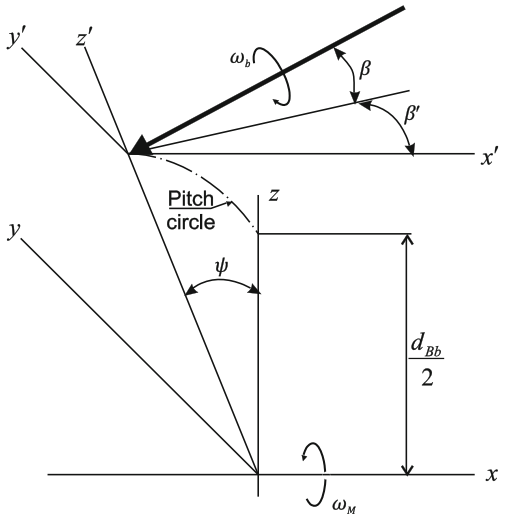

Fig. 3 Ball angular speed vector in a non-zero ball–raceway contact. Redrawn from [14]

$$T_{B\mu s(i/o)} = \frac{3}{8} \mu_b W_{(i/o)} a_{(i/o)} \varepsilon_{(i/o)} \tag{2.17}$$

The variables in Eq. 2.17, except the friction coefficient, μ_b, between the ball and the raceway (steel/steel contact), are explained in detail in the subsequent text. Normal loads, W_o and W_i, on the contact surfaces between the ball and the outer and inner raceways, respectively, are calculated using the following expression (see Fig. 12 for more details):

$$W_{(i/o)} = \frac{F_{Sa}}{N_b \sin\alpha_{(i/o)}} \tag{2.18}$$

where F_{Sa} is the axial force that acts on a bearing (see Fig. 11b) and N_b is the number of the balls in the bearing.

The semi-major axis of the projected contact ellipse, $a_{(i/o)}$, in ball/inner and ball/outer raceway contact zones, respectively, is calculated as [14]

$$a_{(i/o)} = 0.0236 a^*_{(i/o)} \left(\frac{W_{(i/o)}}{\Sigma\rho_{(i/o)}} \right)^{\frac{1}{3}} \tag{2.19}$$

In order to complete the explanation of all variables that occur in Eqs. 2.17 and 2.19, we need to define the following set of geometrical parameters [14]:

- radii of the inner and the outer raceway groove curvatures, respectively: $R_{(i/o)}$
- raceway curvature sum:

$$\sum \rho_{(i/o)} = \frac{1}{d_b} \left(4 - \frac{d_b}{R_{(i/o)}} + \frac{2\gamma_{b(i/o)}}{1 - \gamma_{b(i/o)}} \right) \tag{2.20}$$

– raceway curvature difference:

$$F(\rho)_{i/o} = \frac{\frac{d_b}{R_{(i/o)}} + \frac{2\gamma_{i/o}}{1-\gamma_{i/o}}}{4 - \frac{d_b}{R_{(i/o)}} + \frac{2\gamma_{i/o}}{1-\gamma_{i/o}}} \tag{2.21}$$

– geometrical parameter that defines the ratio between the ball diameter, d_b, and the bearing diameter corresponding to the ball centers, d_{Bb}, projected in the direction of normal load $W_{(i/o)}$:

$$\gamma_{b(i/o)} = \frac{d_b}{d_{Bb}} \cos\alpha_{(i/o)} \tag{2.22}$$

– complete elliptic integral of the second kind on the elliptic contact zones between a ball and inner and outer raceways, respectively:

$$\varepsilon_{(i/o)} = \frac{\pi a^*_{(i/o)} \left(b^*_{(i/o)}\right)^2}{2} \tag{2.23}$$

– dimensionless contact parameters $a^*_{(i/o)}$ and $b^*_{(i/o)}$ that can be obtained as a function of the raceway curvature difference $F(\rho)_{i/o}$ (Eq. 2.21) by interpolating pre-calculated tabular values [14].

Finally, from Eqs. 2.14 and 2.17, we obtain the total power required to overcome the spin-related friction torque for all N_b balls as

$$P_{B\mu s} = N_b \left(T_{B\mu si} + T_{B\mu so}\right)\omega_{spin} \tag{2.24}$$

Equations 2.14–2.23 demonstrate that all variables contributing the power lost due to the ball spinning are dependent either on the spindle speed or on the dynamic contact angles, which are in turn also spindle speed-dependent. Therefore, a numerical simulation is performed to determine a possible model describing the dependency of the power required to overcome the spin-related friction torque on the spindle speed. Power loss due to the spin relation friction in bearings, according to Eq. 2.24, is calculated for spindle speeds up to 20,000 rpm. The calculation is done using a program written in C++. The input parameters for the calculation are taken from the case study given in [22].

Based on the results presented in Fig. 4, the following polynomial model is assumed for the power loss due to the spin-related friction in bearings as a function of the angular speed of the spindle:

$$P_{B\mu s} = K_{0B\mu s}\omega_M + K_{1B\mu s}\omega_M^3 + K_{2B\mu s}\omega_M^5 \tag{2.25}$$

where $K_{0B\mu s}$ and $K_{2B\mu s}$ are constants. The fifth degree term in the polynomial function ensures a better prediction of the power spent due to the spin-related friction during high-speed machining conditions.

2.1.3 Friction torque due to lubricant viscosity, T_{Bv}

The torque due to lubricant viscous friction is given by the following expression [12]:

$$T_{Bv} = \begin{cases} 10^{-7} f_v (\nu n_M)^{\frac{2}{3}} d_{Bb}^3, & \text{if } \nu n_M \geq 2,000 \\ 160 \times 10^{-7} f_v d_{Bb}^3, & \text{if } \nu n_M < 2,000 \end{cases} \tag{2.26}$$

where ν is kinematic viscosity (centistokes), n_M is a spindle (motor shaft) rotational speed (revolutions per minute), and f_v is a factor depending on the type of bearing and method of lubrication (Table 1).

If we limit the domain of application of this model to spindle rotational speeds higher than 2,000 rpm (which should correspond to the kinematic viscosity of the fluid on all working temperatures), we can express the power needed to overcome the torque due to lubricant viscous friction as

$$P_{Bv} = 10^{-7} f_v (\nu n_M)^{\frac{2}{3}} d_{Bb}^3 \omega_M = 10^{-7} f_v \left(\nu \frac{30\omega_M}{\pi}\right)^{\frac{2}{3}} d_{Bb}^3 \omega_M$$

$$\Rightarrow$$

$$P_{Bv} = 4.5 \times 10^{-7} f_v d_{Bb}^3 (\nu)^{\frac{2}{3}} \omega_M^{\frac{5}{3}} \tag{2.27}$$

or, in a simplified way,

$$P_{Bv} = K_{Bv}\omega_M^{\frac{5}{3}} \tag{2.28}$$

where K_{Bv} is the lubricant viscous friction constant.

2.1.4 Windage friction torque, T_{vw}

Another friction source is the air gap between the rotor and stator, i.e., the dynamic viscosity of the air. This problem has been analyzed by Bossmanns and Tu [16]. The rotor and the stator have different surface velocities (the stator has zero surface velocity), and the circumferential velocity profile of

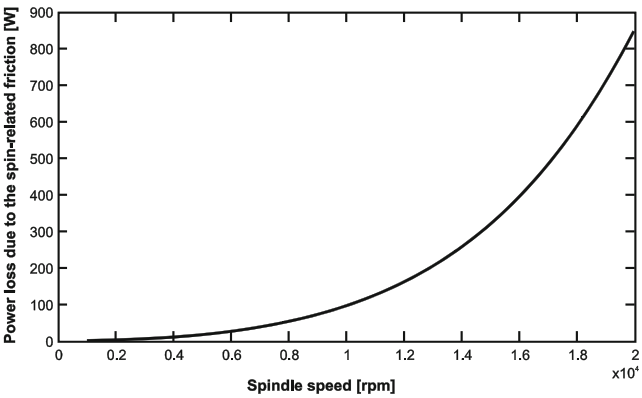

Fig. 4 Power loss due to the spin relation friction in bearings vs. spindle speed

Table 1 Values of f_v depending on ball bearing type and method of lubrication [14]

Type of lubrication	Grease	Oil mist	Oil bath	Oil bath (vertical shaft) or oil jet
f_v	2	1.7	3.3	6.6

air is assumed to be linear between the two boundaries. The velocity gradient and shear stress are therefore assumed to be constant. Shear stress can be computed as [16]

$$\tau = \mu_{\mathrm{Air}} \frac{\partial u}{\partial y} = \mu_{Air} \frac{\omega_M \frac{d_{Rot}}{2}}{h_{\mathrm{Gap}}} \tag{2.29}$$

where $\mu_{\mathrm{Air}}=18.5\times10^{26}$ Ns/m^2 is the dynamic viscosity of air, u is the velocity of air in the circumferential direction (in meters per second), y is the radial coordinate in the gap (in meters), ω_{M} is the spindle (motor shaft) angular velocity (radian per second), d_{Rot} is the rotor diameter (in millimeters), and h_{Gap} is the gap between the rotor and stator (in millimeters).

The additional (*windage friction*) torque, T_{vw}, required for rotation at a given speed is [16]

$$T_{vw} = \frac{d_{Rot}}{2} \int_0^{l_{\mathrm{Rot}}} \tau dA_{\mathrm{rot}} = \frac{\pi d_{\mathrm{Rot}}^3 l_{Rot} \mu_{\mathrm{Air}} \omega_M}{4 h_{\mathrm{Gap}}} \tag{2.30}$$

where:

- A_{Rot} is the cylindrical surface area around the rotor, with a differential:
- $dA_{Rot} = \pi d_{Rot} dl$ (2.31)
- l_{Rot} is the length of the rotor.

Based on Eq. 2.30, the power loss due to the windage friction can be expressed as

$$P_{vw} = T_{vw}\omega_M = \frac{\pi \cdot d_{\mathrm{Rot}}^3 \cdot l_{Rot} \cdot \mu_{\mathrm{Air}}}{4 \cdot h_{Gap}} \cdot \omega_M^2 \tag{2.32}$$

or, in a simplified manner:

$$P_{vw} = K_{vw}\omega_M^2 \tag{2.33}$$

where K_{vw} is the windage friction constant.

2.2 Electrical losses in a motorized spindle

The losses in electric motors originate in several motor components. They are due to very complex phenomena and are dependent on the type, characteristics, and the application of an electric motor. Consequently, in spite of numerous research efforts resulting in various methodologies for analytical or experimental determination of these losses, they still represent a domain where many questions are left unanswered.

According to their sources, electrical losses can be divided into four groups [17]: copper losses in the stator, P_{SCu}; copper losses in the rotor, P_{RCu}; iron losses, P_{MFe}; and stray losses, P_{stray}. Hence, the total losses due to electrical phenomena are calculated as

$$P_{el} = P_{SCu} + P_{RCu} + P_{MFe} + P_{stray} \tag{2.34}$$

2.2.1 Copper losses

Copper losses are a function of the current flowing through the stator winding, I_{S} (amperes), and the rotor cage, I_{R} (amperes). They can be calculated using the following expressions:

$$P_{SCu} = R_{\mathrm{S}} I_{\mathrm{S}}^2 \tag{2.35}$$

$$P_{RCu} = R_{\mathrm{R}} I_{\mathrm{R}}^2 \tag{2.36}$$

where R_{S} and R_{R} (both in ohm) are, respectively, the electric resistances of stator and rotor materials (copper).

An illustration of a typical current–speed curve for a cage induction motor is given in Fig. 5. The form of the curve is similar for both stator and rotor current dependency on speed. From Fig. 5, the following mathematical model corresponding to the current–speed curve ($A_{\mathrm{R/S}}$ and $B_{\mathrm{R/S}}$ are constants depending on the motor type) is defined:

$$I_{R/S} = A_{R/S} - B_{R/S}\omega_M^{-1} \tag{2.37}$$

By introducing Eq. 2.37 into Eqs. 2.35 and 2.36, we get

$$P_{(R/S)Cu} = R_{R/S}\left(A_{R/S} - B_{R/S}\omega_M^{-1}\right)^2 = R_{R/S}\left(A_{\mathrm{R/S}}^2 - 2A_{R/S}B_{R/S}\omega_M^{-1} + B_{\mathrm{R/S}}^2\omega_M^{-2}\right) \Rightarrow$$

$$P_{RCu} = K_{0\mathrm{RCu}} + K_{1\mathrm{RCu}}\omega_M^{-1} + K_{2RCu}\omega_M^{-2} \tag{2.38}$$

$$P_{SCu} = K_{0\mathrm{SCu}} + K_{1\mathrm{SCu}}\omega_M^{-1} + K_{2\mathrm{SCu}}\omega_M^{-2} \tag{2.39}$$

where $K_{0\mathrm{RCu}}$, $K_{1\mathrm{RCu}}$, $K_{2\mathrm{RCu}}$, $K_{0\mathrm{SCu}}$, $K_{1\mathrm{SCu}}$, and $K_{2\mathrm{SCu}}$ are constants.

2.2.2 Iron losses

Iron losses are the result of hysteresis and eddy currents induced in the stator and rotor by the rotating magnetic field.

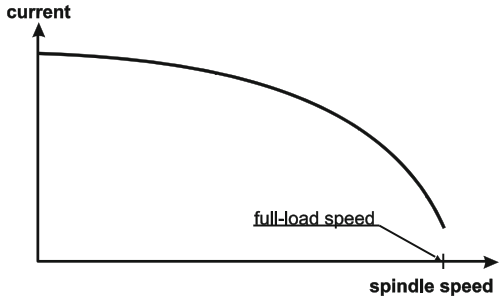

Fig. 5 Current–speed curve for a cage induction motor. Redrawn from [18]

They can be described as a function of the modulating frequency, f, as [19]

$$P_{MFe} = K_{\mathrm{E}} f (3 f_{rated} + f) \tag{2.40}$$

where f_{rated} is the rated frequency (corresponding to the rated voltage of the electromotor) and K_{E} is the eddy current-related constant.

Taking into account that

$$f = n_M \frac{N_p}{60} = \frac{30\omega_M}{\pi}\frac{N_p}{60} = \frac{\omega_M N_p}{2\pi} \tag{2.41}$$

where N_{p} is the number of magnetic pole pairs and n_{M} (in revolutions per minute) is the rotational speed of the motor shaft. Equation 2.40 yields

$$P_{MFe} = K_E 3 f_{rated}\frac{\omega_M N_p}{2\pi} + K_E\left(\frac{\omega_M N_{\mathrm{p}}}{2\pi}\right)^2 \Rightarrow$$

$$P_{MFe} = K_{1\mathrm{MFe}}\omega_M + K_{2\mathrm{MFe}}\omega_M^2 \tag{2.42}$$

where $K_{1\mathrm{MFe}}$ and $K_{2\mathrm{MFe}}$ are the constants.

2.2.3 Stray losses

Stray losses represent the same phenomenon as iron losses, but due to the spindle parts outside the motor that are located in the area reached by the magnetic field. These losses are also frequency-dependent, but they are difficult to calculate. There are several methodologies to determine them experimentally or estimate them by performing a finite element analysis [20].

An experimental analysis by Agamloh [21], conducted on about a thousand 60-Hz induction motors, has determined an average stray power loss at 1.2 % of useful power, P_{cut} (invested in overcoming the cutting torque)

$$P_{stray} = 0.012 P_{\mathrm{cut}} \tag{2.43}$$

2.3 Model synthesis

Table 2 gives a review of the expressions presented in Sections 2.1 and 2.2 which provide the dependency of different sources of power loss in a motorized spindle drive.

The total spindle power is given by Eq. 2.3, which is expressed in detail as

$$\begin{aligned} P_{ACeff} = {} & K_{\mathrm{B}\mu\mathrm{l}}\omega_M + K_{0\mathrm{B}\mu\mathrm{s}}\omega_M + K_{1\mathrm{B}\mu\mathrm{s}}\omega_M^3 + K_{2\mathrm{B}\mu\mathrm{s}}\omega_M^5 + K_{\mathrm{B}\nu}\omega_M^{\frac{5}{3}} + \\ & + K_{\nu\mathrm{w}}\omega_M^2 + K_{0\mathrm{RCu}} + K_{1\mathrm{RCu}}\omega_M^{-1} + K_{2\mathrm{RCu}}\omega_M^{-2} + K_{0\mathrm{SCu}} \\ & + K_{1\mathrm{SCu}}\omega_M^{-1} + \\ & + K_{2\mathrm{SCu}}\omega_M^{-2} + K_{1\mathrm{MFe}}\omega_M + K_{2\mathrm{MFe}}\omega_M^2 + 0.012 P_{cut} + P_{cut} \end{aligned} \tag{2.44}$$

and spindle current proportional to the total spindle power, from Eqs. 1.1 and 2.44, is given as

$$\begin{aligned} I = {} & K_{lm}K_{2\mathrm{B}\mu\mathrm{s}}\omega_M^5 + K_{lm}K_{1\mathrm{B}\mu\mathrm{s}}\omega_M^3 + K_{lm}(K_{\nu\mathrm{w}} + K_{2\mathrm{MFe}})\omega_M^2 \\ & + K_{lm}K_{\mathrm{B}\nu}\omega_M^{\frac{5}{3}} + K_{\mathrm{lm}}(K_{\mathrm{B}\mu\mathrm{l}} + K_{0\mathrm{B}\mu\mathrm{s}} + K_{1\mathrm{MFe}})\omega_M \\ & + K_{lm}(K_{1RCu} + K_{1\mathrm{SCu}})\omega_M^{-1} + K_{lm}(K_{2\mathrm{RCu}} + K_{2\mathrm{SCu}})\omega_M^{-2} \\ & + K_{lm}(K_{0\mathrm{RCu}} + K_{0\mathrm{SCu}}) + K_{lm}1.012 T_{cut}\omega_M \end{aligned} \tag{2.45}$$

For air cutting (T_{cut}=0), the measured spindle motor current accounts only for the losses in the spindle drive. Hence, Eq. 2.45 becomes

$$\begin{aligned} I_f = {} & K_{lm}K_{2\mathrm{B}\mu\mathrm{s}}\omega_M^5 + K_{lm}K_{1\mathrm{B}\mu\mathrm{s}}\omega_M^3 + K_{lm}(K_{\nu\mathrm{w}} + K_{2\mathrm{MFe}})\omega_M^2 \\ & + K_{lm}K_{\mathrm{B}\nu}\omega_M^{\frac{5}{3}} + + K_{lm}(K_{\mathrm{B}\mu\mathrm{l}} + K_{0\mathrm{B}\mu\mathrm{s}} + K_{1\mathrm{MFe}})\omega_M \\ & + K_{lm}(K_{1RCu} + K_{1\mathrm{SCu}})\omega_M^{-1} + + K_{lm}(K_{2\mathrm{RCu}} + K_{2SCu})\omega_M^{-2} \\ & + K_{lm}(K_{0\mathrm{RCu}} + K_{0\mathrm{SCu}}) \end{aligned} \tag{2.46}$$

The different constants in Eq. 2.46 are combined and the resulting expression is given by

$$\begin{aligned} I_{\mathrm{f}} = {} & a_1\omega_M^5 + a_2\omega_M^3 + a_3\omega_M^2 + a_4\omega_M^{\frac{5}{3}} + \\ & + a_5\omega_M + a_6\omega_M^{-1} + a_7\omega_M^{-2} + a_8 \end{aligned} \tag{2.47}$$

Equation 2.45 is rewritten as

$$I = I_{\mathrm{f}} + K_{lm}\cdot 1.012 T_{\mathrm{cut}}\omega_M \tag{2.48}$$

3 Development of an empirical model for cutting torque prediction

MIKRON HPM 600U, a five-axis milling machine equipped with the controller iTNC530, is used for experimentation purposes. A flat end mill of 20 mm diameter with two flutes is used as cutting tool. The material of the workpiece is Certal

Table 2 Power loss components in a motorized spindle drive

Power loss component	Expression	Equation no.
Power needed to overcome the bearing friction torque due to applied load	$P_{B\mu l} = K_{B\mu l}\omega_M$	2.8
Power needed to overcome the spin-related friction torque	$P_{B\mu s} = K_{0B\mu s}\omega_M + K_{1B\mu s}\omega_M^3 + K_{2B\mu s}\omega_M^5$	2.25
Power needed to overcome the torque due to lubricant viscous friction	$P_{Bv} = K_{Bv}\omega_M^{\frac{5}{3}}$	2.28
Power loss due to windage friction torque	$P_{vw} = K_{vw}\omega_M^2$	2.33
Rotor copper loss	$P_{RCu} = K_{0RCu} + K_{1RCu}\omega_M^{-1} + K_{2RCu}\omega_M^{-2}$	2.38
Stator copper loss	$P_{SCu} = K_{0SCu} + K_{1SCu}\omega_M^{-1} + K_{2SCu}\omega_M^{-2}$	2.39
Iron loss	$P_{MFe} = K_{1MFe}\omega_M + K_{2MFe}\omega_M^2$	2.42
Stray losses	$P_{stray} = 0.012P_{cut}$	2.43

(AlZnMgCu 0.5). The data acquisition platform is developed in LabVIEW 2010. The cutting torque dynamometer (Kistler 9125A) and the measurement platform are shown in Fig. 6. The constants, a_i (i=1, 2…8), in Eq. 2.47, are identified with air cutting experiments performed at different spindle speeds. The spindle speed is varied from 500 to 20,000 rpm, with an increment of 500 rpm. Spindle motor current is acquired directly from the machine controller. By using MATLAB 2010a as the programming environment, the developed model is fitted to the measured spindle motor current and the values of a_i are calculated.

The obtained values of constants a_i, corresponding to the model given in Eq. 2.47, are:

$$\left.\begin{aligned} a_1 &= 4.98\cdot10^{-22}\left[\tfrac{A}{rpm^5}\right] & a_5 &= -1.21\cdot10^{-12}\left[\tfrac{A}{rpm}\right]\\ a_2 &= -1.73\cdot10^{-13}\left[\tfrac{A}{rpm^3}\right] & a_6 &= 2.76\cdot10^{-08}[A\cdot rpm]\\ a_3 &= 5.11\cdot10^{-9}\left[\tfrac{A}{rpm^2}\right] & a_7 &= -6.33\cdot10^{-05}[A\cdot rpm^2]\\ a_4 &= 3.25\cdot10^{-10}\left[\tfrac{A}{rpm^{5/3}}\right] & a_8 &= 0.1410 \end{aligned}\right\} \quad (3.1)$$

Although a_i has a very small value, its combined effect with ω_M (in revolutions per minute) at a high spindle speed cannot be ignored. It helps ensure the accurate prediction of the developed model at higher spindle speeds.

After introducing the values of constants a_i, Eq. 2.46 becomes

$$\begin{aligned} I_f = {} & 4.98\times10^{-22}\omega_M^5 - 1.73\times10^{-13}\omega_M^3 + 5.11\times10^{-9}\omega_M^2\\ & +3.25\times10^{-10}\omega_M^{5/3} - 1.21\times10^{-12}\omega_M + 2.76\times10^{-8}\omega_M^{-1}\\ & -6.33\times10^{-5}\omega_M^{-2} + 0.1410 \end{aligned} \quad (3.2)$$

The comparison of results, presented in Fig. 7, clearly shows better compliance of the developed model to the experimental data than Dunwoody's model [9], presented in Eq. 1.3.

The load meter constant, K_{lm}, is identified with slot cutting experiments performed at different spindle speeds. Spindle speed is varied from 1,000 to 20,000 rpm, with an increment of 1,000 rpm. The stable axial depth of cut (2 mm) and feed (0.1 mm/flute) are kept constant during the experiments. Cutting torque (T_{cut}) is measured with a cutting torque dynamometer (Kistler 9125A), while the spindle current corresponding to the total spindle power (I) is acquired directly from the machine controller. On the other hand, the spindle current proportional to the power loss (I_f) is calculated from Eq. 3.2.

The measured values of the total spindle motor current (I) and the calculated spindle motor current corresponding to the power spent for cutting ($I-I_f$) are presented in Fig. 8a. The percentage of total losses, $(I_f\cdot100)/I$, is presented in Fig. 8b. The plots demonstrate that the total losses are quite significant, especially at high spindle speeds.

Subsequently, from Eq. 2.48, we get

$$\frac{I-I_f}{1.012T_{cut}} = K_{lm}\omega_M \quad (3.3)$$

The load meter constant, K_{lm}, is estimated by linear regression of the $\frac{I-I_f}{1.012T_{cut}}$ values, and the fitted line is presented as a solid line, as shown in Fig. 9.

The values of the spindle motor current at lower spindle speeds are not reliable, as can be seen in Fig. 8a, because they are too small to be accurately measured by the load meter. After excluding the data corresponding to spindle speeds smaller than 4,000 rpm (see Fig. 9), the obtained value of K_{lm} is 1.9973×10^{-4} A/W.

By rewriting the complete model (Eq. 2.45) as

$$\begin{aligned} I = {} & 4.98\cdot10^{-22}\omega_M^5 - 1.73\times10^{-13}\omega_M^3 + 5.11\times10^{-9}\omega_M^2\\ & +3.25\times10^{-10}\omega_M^{5/3} - 1.21\times10^{-12}\omega_M + 2.76\times10^{-8}\omega_M^{-1}\\ & -6.33\times10^{-5}\omega_M^{-2} + 0.1410 + 1.012\cdot1.9973\times10^{-4}T_{cut}\omega_M \end{aligned} \quad (3.4)$$

From Eq. 3.4, the developed model to estimate the cutting torque from the spindle motor current obtains its final expression as

$$T_{cut} = \frac{I-4.98\times10^{-22}\omega_M^5+1.73\times10^{-13}\omega_M^3-5.11\times10^{-9}\omega_M^2-3.25\times10^{-10}\omega_M^{5/3}}{1.012\cdot1.9973\times10^{-4}\omega_M} + \frac{1.21\times10^{-12}\omega_M-2.76\times10^{-8}\omega_M^{-1}+6.33\times10^{-5}\omega_M^{-2}-0.1410}{1.012\cdot1.9973\times10^{-4}\omega_M} \quad (3.5)$$

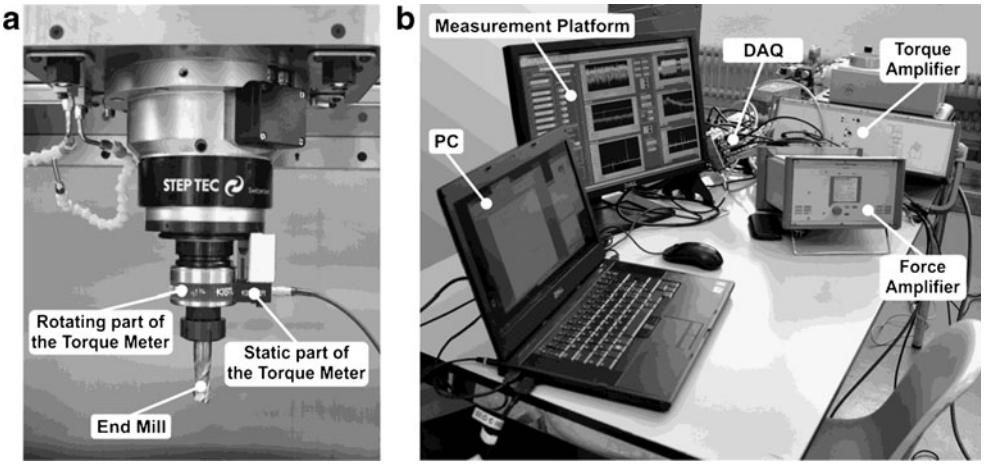

Fig. 6 Experimental setup. **a** Cutting torque dynamometer mounting. **b** Data acquisition platform

Cutting torque (Eq. 3.5) is defined as a function of spindle speed (revolutions per minute) and spindle motor current (ampere), which in turn is load-dependent. It is probable that the load meter constant depends on the given combination of workpiece material and tool geometry. It is, however, still to be determined how significant this influence is.

4 Validation and implementation of the developed cutting torque model

In the previous section, it has been demonstrated that the developed model of the spindle power predicts the total power losses accurately. The next objective is to validate experimentally the developed cutting torque prediction model (Eq. 3.5) and propose its industrial application for tangential cutting force coefficient identification.

Cutting force coefficients are identified by performing slot cutting experiments at different feed rates. The feed rate is varied from 0.04 to 0.18 mm/flute, with an increment of 0.02 mm/flute. Stable axial depth of cut (4 mm) and spindle speed (7000 rpm) are kept constant during the slot cutting experiments. Spindle motor current is acquired from the controller, and then the cutting torque is estimated with the developed model (Eq. 3.5). For validation of the developed cutting torque prediction model, the cutting torque is also measured directly with the cutting torque dynamometer. The results presented in Fig. 10 validate that the cutting torque predicted with the developed model is in good compliance with the measured cutting torque values. The same data will also be used to identify the tangential cutting force coefficients.

The tangential cutting force per unit depth of cut along the cutting edge j of an end mill is given by Altintas [23]

$$dF_{t,j}(\phi) = K_{tc}h(\phi) + K_{te} \tag{4.1}$$

Here, ϕ is the immersion angle, K_{tc} is the tangential cutting force coefficient contributed by shearing action, K_{te} is the tangential edge force coefficient, and $h(\phi)$ is the chip thickness which is given by

$$h(\phi) = f_t \sin(\phi) \tag{4.2}$$

where f_t is the feed rate in (millimeters per flute). The instantaneous cutting torque can be calculated as

$$dT_{c,j}(\phi) = R(K_{tc}h(\phi) + K_{te})g(\phi) \tag{4.3}$$

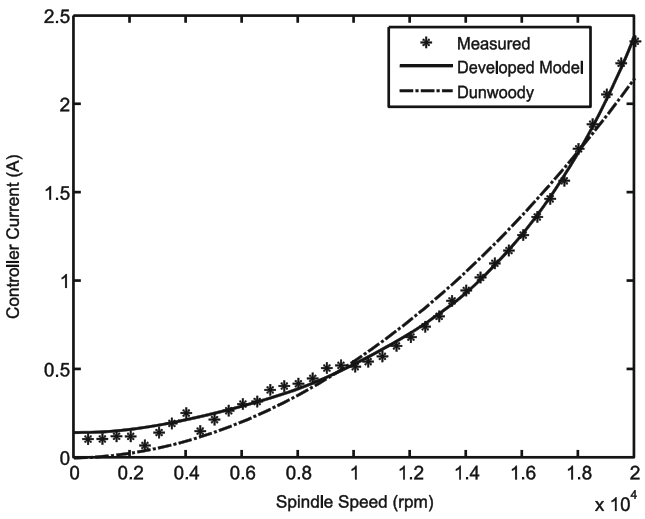

Fig. 7 Air cutting experimental results

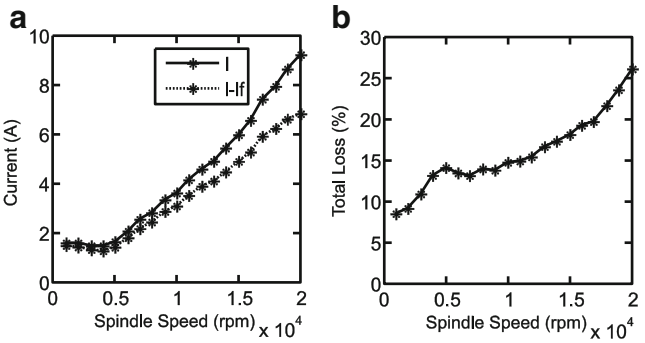

Fig. 8 Illustration of the total power loss dependency. **a** Spindle speed vs. current. **b** Spindle speed vs. total losses

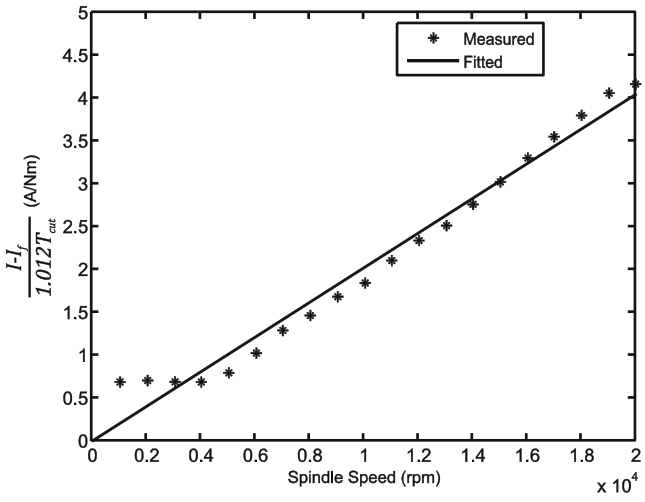

Fig. 9 Slot cutting experimental results

where R is the radius of the milling tool and $g(\phi)$ is a function which is unity while the tooth is in the cutting zone and zero when the tooth is out of the cutting zone.

The average torque per unit depth of cut is given by

$$d\overline{T}_{c,j} = \frac{R}{2\pi}\int_0^{2\pi} g(\phi)[(K_{tc}f_t\sin(\phi) + K_{te})] \tag{4.4}$$

For slot cutting tests

$$g(\phi) = \begin{cases} 1 \text{ if } 0 \le \phi < \pi \\ 0 \text{ if } \pi \le \phi < 2\pi \end{cases} \tag{4.5}$$

The average torque per unit depth of cut, for a single flute, is expressed as [9]

$$d\overline{T}_{c,j} = \frac{RK_{tc}}{\pi}f_t + \frac{RK_{te}}{2} \tag{4.6}$$

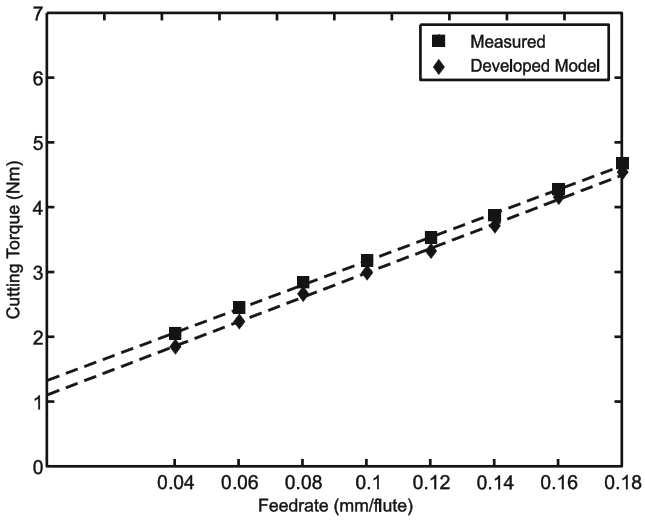

Fig. 10 Average cutting torque values

Total average torque, for all cutting flutes and given depth of cut (a), is given by

$$\overline{T}_c = \frac{RNaK_{tc}}{\pi}f_t + \frac{RNaK_{te}}{2} \tag{4.7}$$

The cutting and edge components ($\frac{RNaK_{tc}}{\pi}$, $\frac{RNaK_{te}}{2}$) are estimated by a linear regression of the cutting torque values as presented in Fig. 10. Tangential force coefficients are identified from the direct measurement of cutting torque by a torque dynamometer and also from the estimated values of cutting torque from the developed model. The comparison of the results is presented in Table 3.

Edge force coefficient (K_{te}) has a negligible effect on the cutting forces and has no effect on chatter-free region prediction [23]; therefore, 16.56 % error in its determination is quite acceptable. On the other hand, precise identification of the tangential cutting coefficient, K_{tc}, is indispensable for an accurate prediction of cutting forces and chatter-free regions. The difference between the tangential cutting coefficients identified from the predicted and experimentally measured cutting torque is only 2.34 %, which represents another validation of the accuracy of the developed model for industrial application.

5 Conclusion

In this paper, an enhanced procedure for cutting torque determination and tangential cutting force coefficient identification from the spindle motor current is presented. The spindle motor current, obtained from the integrated load meter, is proportional to the total spindle power. The cutting torque is obtained from the difference of spindle power consumption in material and air cutting by using a methodology that required the development of a mathematical spindle power model. Finally, the tangential cutting coefficients are identified from such obtained cutting torque. This procedure demonstrates several salient features compared to previous approaches.

The developed model of spindle power considers all mechanical and electrical sources of power losses in the spindle motor. Mechanical losses (load-related friction in spindle bearings, spin-related friction, friction due to lubricant viscosity, and windage friction) and electrical losses (rotor and stator copper loss, iron loss, and stray losses) are

Table 3 Tangential force coefficients identified from the measured and the predicted cutting torque

Coefficient	Measured	Predicted	% Error
K_{tc} (N/mm^2)	726	743	2.34
K_{te} (N/mm)	33.2	27.8	16.26

all taken into account during the model development and expressed as a function of spindle rotational speed and load.

Furthermore, an empirical model for cutting torque prediction has been developed from the results of air cutting and slot cutting experiments at different spindle speeds. It has been demonstrated that the developed model predicts the spindle power losses accurately. The predicted values of the cutting torque using the developed empirical model are additionally validated by the simultaneous direct measurement of cutting torque from a cutting torque dynamometer. The results have demonstrated good compliance of the predicted cutting torque with the one obtained in the direct measurement, thus proving the accurate identification of tangential cutting force coefficients.

The developed procedure is very suitable for shop floor implementation. It eliminates the need for a costly and complex external hardware setup as it uses the data already available in CNC units. Machine tool manufacturers can implement the developed model in CNC units and make the cutting torque available to the end user in the form of a built-in database of load meter constants for different workpiece material/tool geometry combinations. This would represent a substantial step toward accomplishing the idea of smart machining. Optimally selected cutting conditions, based on the results of the predicted chatter-free regions and cutting force, will ensure enhancement in the overall productivity of the milling process.

Acknowledgments The experiments, carried out in the framework of CTI project no. 10008.1 PFES-ES, were supported by Federal Department of Economic Affairs, Switzerland. We would like to take the opportunity to thank Mr. David Schranz from Mikron Agie Charmilles AG and Dr. Oliver Avram from EPFL for their valuable contributions during the experiments. We also thank Mr. Jean-Philippe Besuchet from Mikron Agie Charmilles AG for his collaboration and feedback throughout the work.

Appendix

Calculation of dynamic values of bearing contact angles

In Fig. 11a, free-state (nominal) value of the bearing contact angle (α_f) is illustrated. This condition refers to when the bearing is immobile and there is no preload. The outer (inner) contact angle is the one that the line connecting the contact point A on the outer ring (B on the inner ring) and the center of the ball forms with the normal direction to the bearing axis.

In free-state conditions, both inner and outer contact angles have the same value, equal to α_f. The free-state angle of the bearing, a_f, is defined by the following trigonometric expression:

$$\cos\alpha_f = \frac{t - \frac{P_d}{2}}{t} \tag{5}$$

where:

- t is the distance between the centers of the curvature of the inner and the outer raceway grooves, which is equal to:

$$t = R_o + R_i - d_b \tag{6}$$

- R_o and R_i are, respectively, the radii of the outer and the inner raceway groove curvatures.
- P_d is the diametric clearance, which is, by definition [14]

$$P_d = d_{Bo} - d_{Bi} - 2d_b = 2(b_1 + b_2) \tag{7}$$

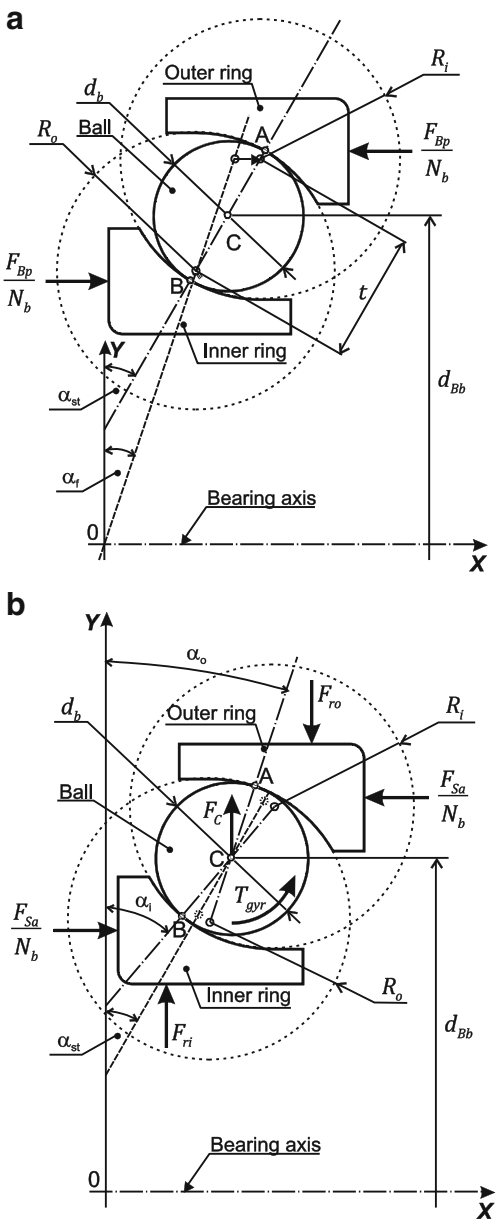

Fig. 11 Free-state, static (**a**) and dynamic (**b**) values of the bearing contact angle. Redrawn from [15]

- d_{Bo} and d_{Bi} are the outer and inner ring raceway contact diameters (in millimeters), respectively
- d_b is the ball diameter (in millimeters)
- b_1 and b_2 are clearances between the ball and the raceways (in millimeters)

Figure 11a also depicts the condition where the bearing is still immobile, but there is a static preload, F_{Bp}, in the axial direction. An assumption is made that this load is equally distributed on each of the balls, where N_b stands for their number. Under the preload, the inner ring moves with respect to the outer ring in the direction of the bearing axis, X. Both contact points and the center of the ball are still collinear, but the angle (α_{st}) that this line forms with the direction normal to the bearing axis (Y) is greater than the free-state angle, α_f.

The static value of the bearing contact angle, α_{st}, can be calculated using the following expression [14]:

$$\frac{F_{Bp}}{N_b K_a d_b^{2n-1}} = \sin\alpha_{st}\left(\frac{\cos\alpha_f}{\cos\alpha_{st}} - 1\right)^n \tag{8}$$

where K_a is the axial deflection constant (in megapascals) that can be obtained from the corresponding experimentally determined diagrams [14] as a function of the total curvature B

$$B = \frac{R_o}{d_b} + \frac{R_i}{d_b} - 1 \tag{9}$$

Equation 8 can be solved numerically by the Newton–Raphson method. The equation to be satisfied iteratively is

$$\alpha'_{st} = \alpha_{st} + \frac{\frac{F_{Bp}}{N_b K_a d_b^{2n-1}} - \sin\alpha_{st}\left(\frac{\cos\alpha_f}{\cos\alpha_{st}} - 1\right)^n}{\cos\alpha_{st}\left(\frac{\cos\alpha_f}{\cos\alpha_{st}} - 1\right)^n + n\tan^2\alpha_{st}\left(\frac{\cos\alpha_f}{\cos\alpha_{st}} - 1\right)^{n-1}\cos\alpha_f} \tag{10}$$

which is satisfied when $\alpha'_{st} - \alpha_{st}$ is zero.

The main case that we are interested in is related to the dynamic state, when the bearing rotates under the load. The load on a bearing consists of an axial force, F_{Sa}, equally distributed on each of N_b balls and radial forces, F_{ro} and F_{ri}, that act on a ball through the outer and inner rings, respectively (Fig. 11b). The assumptions made are that the bearing has a constant rotational speed around the X-axis, the motion is without vibrations, and no sliding motion is supposed to appear at points A and B [15].

Balls follow the cage orbital motion around the X-axis. Due to friction forces in contact points, each ball also rotates around its own axis. This leads to the occurrence of the gyroscopic moments on the balls (Fig. 12a). Because of the inertial force (centrifugal force, F_C, in Fig. 12a), the outer and inner contact angles have now two different values, α_o and α_i.

In order to calculate the bearing contact angles, a free body diagram is constructed in Fig. 12a. At the contact points A and B, the outer and inner contact actions are

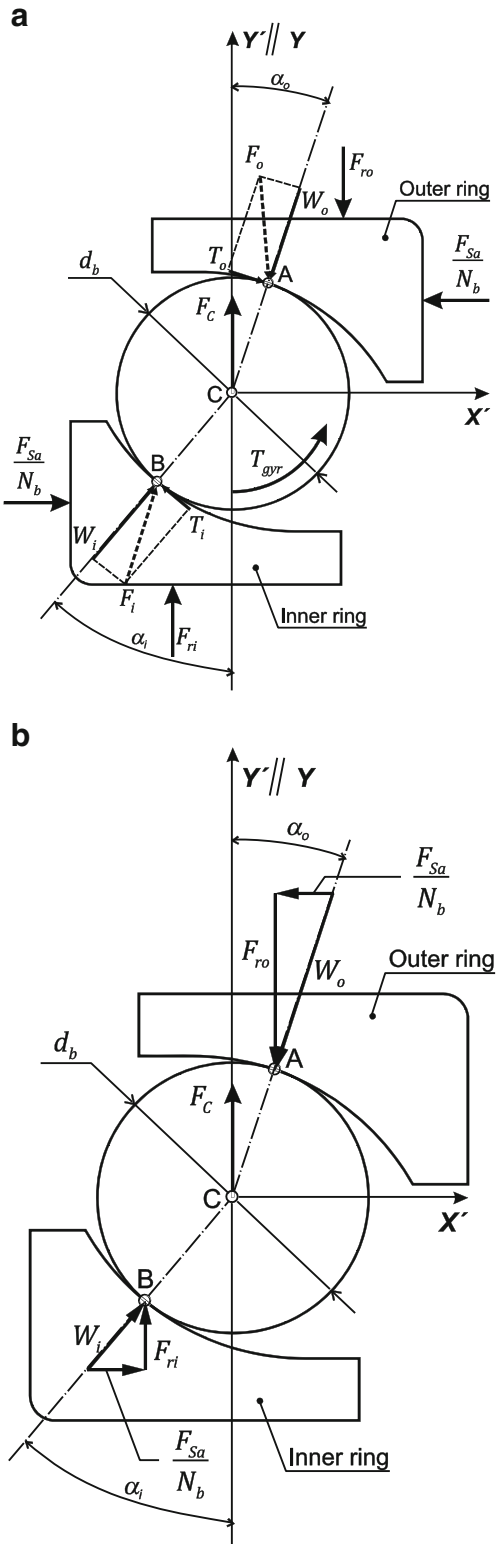

Fig. 12 Free body diagram of an angular contact ball bearing. Redrawn from [14]

supposed to be reduced to the resultant forces F_o and F_i (acting on each ball). These forces are decomposed, respectively, into normal loads, W_o and W_i, and tangential loads, T_o and T_i. The result of the centrifugal force, F_C, is directed along the *Y*-axis and is applied at point C (center of the ball).

The assumption that the tangential forces compensate the gyroscopic moment allows for a simplification of the free body diagram [15]. Thus, we get the system of forces represented in Fig. 12b, which will help us determine the set of equations necessary for the calculation of contact angles.The sum of force projections in direction Y' is

$$F_{ri} - F_{ro} + F_C = 0 \tag{11}$$

From Fig. 12b, we also get

$$\tan\alpha_i = \frac{\frac{F_{Sa}}{N_b}}{F_{ri}} \Rightarrow F_{ri} = \frac{F_{Sa}}{N_b \tan\alpha_i} \tag{12}$$

$$\tan\alpha_o = \frac{\frac{F_{Sa}}{N_b}}{F_{ro}} \Rightarrow F_{ro} = \frac{F_{Sa}}{N_b \tan\alpha_o} \tag{13}$$

By introducing Eqs. 12 and 13 into Eq. 11, we get

$$F_{ri} - F_{ro} + F_C = \frac{F_{Sa}}{N_b \tan\alpha_i} - \frac{F_{Sa}}{N_b \tan\alpha_o} + F_C = 0 \Rightarrow$$

$$\frac{1}{\tan\alpha_o} - \frac{1}{\tan\alpha_i} = \frac{F_C \cdot N_b}{F_{Sa}} \tag{14}$$

where:

- F_C is the centrifugal force (in newton) which can be calculated as [19] (p. 175)

$$F_C = \frac{\pi \rho_b d_b^3 \omega_C^2 d_{Bm}}{12} \tag{15}$$

- ρ_b is the mass density of balls/rollers (in kilograms per cubic meter)
- ω_C is the angular velocity of the cage (radian per second)

$$\omega_C = \frac{2\pi n_C}{60} = \frac{\pi n_C}{30} \tag{16}$$

- n_C (1/s) is the rotational speed of the cage (orbital ball/roller speed) [14]

$$n_C = \frac{1}{2}[n_i(1-\gamma_b) + n_o(1+\gamma_b)] \tag{17}$$

- n_o and n_i are the rotational speeds of the outer and inner rings, respectively
- γ_b is a geometrical parameter

$$\gamma_b = \frac{d_b \cos\alpha_{st}}{d_{Bm}} \tag{18}$$

For machine tools, n_o=0 and Eq. 17 becomes

$$n_C = \frac{n_i}{2}(1-\gamma_b) = n_C = \frac{n_M}{2}(1-\gamma_b) \tag{19}$$

where n_M is the number of rotations of the spindle shaft.

Bossmanns [19] makes an assumption that the changes of the contact angles in the outer and inner contact points follow the rules:

$$\alpha_o = \alpha_{st} + \Delta\alpha_o \tag{20}$$

$$\alpha_i = \alpha_{st} + \Delta\alpha_i \tag{21}$$

$$\Delta\alpha_o = -\Delta\alpha_i \tag{22}$$

which leads to the conclusion

$$\alpha_o + \alpha_i = 2\alpha_{st} \tag{23}$$

Equations 10 and 23 constitute a sufficient system for the calculation of the dynamic load contact angles, which can be solved by numerical iteration.

References

1. Altintas Y, Weck M (2004) Chatter stability of metal cutting and grinding. CIRP Ann Manuf Technol 53(2):619–642
2. Quintana G, Ciurana J (2011) Chatter in machining processes: a review. Int J Mach Tool Manuf 51(5):363–376
3. Altintas Y, Budak E (1995) Analytical prediction of stability lobes in milling. CIRP Ann Manuf Technol 44(1):357–362
4. Zhang Z, Zheng L, Zhang L, Li Z, Liu D, Zhang B (2005) A study on calibration of coefficients in end milling forces model. Int J Adv Manuf Technol 25(7–8):652–662
5. Wang H, Qin X, Ren C, Wang Q (2012) Prediction of cutting forces in helical milling process. Int J Adv Manuf Technol 58:849–859
6. Budak E, Altintas Y (1994) Peripheral milling conditions for improved dimensional accuracy. Int J Mach Tool Manuf 34 (7):907–918
7. Matsubara A, Ibaraki I (2009) Monitoring and control of cutting forces in machining processes: a review. International Journal of Automation Technology 3(4):445–456
8. Cho DW, Jeong YH (2002) Estimating cutting force from rotating and stationary feed motor currents on a milling machine. Int J Mach Tool Manuf 42(14):1559–1566
9. Dunwoody K (2010) Automated identification of cutting force coefficients and tool dynamics on CNC machines. University of British Columbia, Vancouver
10. Cao YZ, Altintas Y (2004) A general method for the modeling of spindle-bearing systems. J Mech Des 126(6):1089–1104. doi:10.1115/1.1802311
11. Jones AB (1960) A general theory for elastically constrained ball and radial roller bearings under arbitrary load and speed conditions. ASME J Basic Eng 82:309–320
12. Palmgren A (1964) Grundlagen der Wälzlagertechnik, 3rd edn. Franckische Verlagshandlung, Stuttgart
13. Houpert L (1997) A uniform analytical approach for ball and roller bearings calculations. J Tribol—T Asme 119(4):851–858

14. Harris TA (2001) Rolling bearing analysis, 4th edn. Wiley-Interscience, New York
15. Antoine JF, Abba G, Molinari A (2006) A new proposal for explicit angle calculation in angular contact ball bearing. J Mech Des 128(2):468–478. doi:10.1115/1.2168467
16. Bossmanns B, Tu JF (2001) A power flow model for high speed motorized spindles—heat generation characterization. J Manuf Sci Eng—Trans ASME 123(3):494–505
17. Jordan HE (1994) Energy-efficient electric motors and their applications, 2nd edn. Plenum, New York
18. Hughes A (2006) Electric motors and drives: fundamentals, types and applications, 3rd edn. Elsevier, Amsterdam
19. Bossmanns B (1997) Thermo mechanical modeling of motorized spindle systems for high speed milling. Purdue University, West Lafayette
20. Köfler H (2003) Stray load losses in induction machines. A review of experimental measuring methods and a critical performance evaluation. Paper presented at the International Conference on Renewable Energy and Power Quality (ICREPQ)
21. Agamloh EB (2010) An evaluation of induction machine stray load loss from collated test results. IEEE Transactions on Industry Applications 46(6):2311–2318
22. Avram IO (2010) Machine tool use phase: modeling and analysis with environmental considerations. Swiss Federal Institute of Technology Lausanne, Lausanne
23. Altintas Y (2000) Manufacturing automation: metal cutting mechanics, machine tool vibrations and CNC design. Cambridge University Press, Cambridge